

# Foreshock sequences and short-term earthquake predictability on East Pacific Rise transform faults

Jeffrey J. McGuire<sup>1</sup>, Margaret S. Boettcher<sup>2</sup> & Thomas H. Jordan<sup>3</sup>

<sup>1</sup>Department of Geology and Geophysics, Woods Hole Oceanographic Institution, and <sup>2</sup>MIT-Woods Hole Oceanographic Institution Joint Program, Woods Hole, Massachusetts 02543-1541, USA

<sup>3</sup>Department of Earth Sciences, University of Southern California, Los Angeles, California 90089-7042, USA

**East Pacific Rise transform faults are characterized by high slip rates (more than ten centimetres a year), predominately aseismic slip and maximum earthquake magnitudes of about 6.5. Using recordings from a hydroacoustic array deployed by the National Oceanic and Atmospheric Administration, we show here that East Pacific Rise transform faults also have a low number of aftershocks and high foreshock rates compared to continental strike-slip faults. The high ratio of foreshocks to aftershocks implies that such transform-fault seismicity cannot be explained by seismic triggering models in which there is no fundamental distinction between foreshocks, mainshocks and aftershocks. The foreshock sequences on East Pacific Rise transform faults can be used to predict (retrospectively) earthquakes of magnitude 5.4 or greater, in narrow spatial and temporal windows and with a high probability gain. The predictability of such transform earthquakes is consistent with a model in which slow slip transients trigger earthquakes, enrich their low-frequency radiation and accommodate much of the aseismic plate motion.**

On average, before large earthquakes occur, local seismicity rates show a significant increase<sup>1</sup>. In continental regions, where dense regional seismic networks provide the best data, most foreshock studies<sup>2–4</sup>, though not all<sup>5</sup>, are consistent with the hypotheses that earthquake nucleation is independent of magnitude and that foreshocks result from a general triggering process in which there is no fundamental distinction between foreshocks, mainshocks and aftershocks. The inability to distinguish foreshocks from the statistical fluctuations in the continental background seismicity severely limits their usefulness in predicting large earthquakes<sup>6</sup>.

It is unclear, however, whether these statements apply to other tectonic environments, or how aseismic processes affect earthquake triggering. Aseismic slip transients with timescales of days to months have recently been observed in the subduction zones of Japan<sup>7–9</sup> and Cascadia<sup>10</sup>, using continuously monitored GPS arrays. The possibility that aseismic slip triggers large earthquakes on subduction megathrusts is especially intriguing given the observation<sup>11</sup> that a slow slip transient occurred 15 minutes before the great 1960 Chilean megathrust earthquake, which had a moment magnitude ( $M_w$ ) of 9.5, the largest ever recorded. Notably, subduction zones are observed to have higher foreshock rates than continental regions<sup>12</sup>.

Another tectonic environment in which aseismic processes are thought to exert a strong influence on fault behaviour is mid-ocean ridge transform faults (RTFs). Studies over the last several decades<sup>13–15</sup> have shown that on average most of the slip on RTFs, up to about 85% (ref. 15), is aseismic. Moreover, the seismic component of slip occurs in earthquakes that are relatively small ( $M_w \leq 7.2$ ) given the length of the faults<sup>14–16</sup>. Many of the larger RTF earthquakes are slow events with anomalous low-frequency radiation<sup>17,18</sup>. Low-frequency spectral analyses<sup>19,20</sup> have indicated that slow RTF earthquakes are compound events comprising an ordinary rupture and a slow transient of comparable moment but much longer duration; in some cases, the slow component precedes, and presumably initiates, the main seismic component. Time-domain records of slow precursors to RTF earthquakes<sup>20,21</sup> and episodes of coupled seismic slip observed on adjacent RTFs<sup>20,22</sup>

support the inference of slow slip transients, but the subject remains controversial<sup>23</sup>.

## Hydroacoustic detection of foreshocks

Here we use data from a six-element hydroacoustic array deployed by the National Oceanic and Atmospheric Administration's Pacific Marine Environmental Laboratory (NOAA-PMEL) to examine anomalous foreshock sequences on East Pacific Rise (EPR) transform faults (Fig. 1). The NOAA-PMEL arrays<sup>24–26</sup> routinely locate EPR earthquakes with acoustic source level (ASL) magnitudes (see Methods)  $M_{ASL}$  below 3, reducing the detection threshold by 1.5–2.0 magnitude units below global seismicity catalogues (see Methods). A reconnaissance study indicated that foreshocks in the last hour before large events are significantly more common on EPR transform faults than on strike-slip faults in the North Atlantic, Northeast Pacific or Southern California<sup>27</sup>.

Figure 2 displays stacks of the seismicity in space-time windows centred on nine mainshocks that occurred on the Discovery and Gofar transform faults between May 1996 and December 2001. This set of mainshocks comprised all  $M_w \geq 5.4$  earthquakes on these two faults recorded by the NOAA-PMEL array in the Harvard Centroid Moment Tensor (CMT) catalogue<sup>28</sup> that did not follow within 1 week and 100 km of another mainshock. The longer window (Fig. 2a) shows low background seismicity tens of hours before the mainshocks and the subsequent aftershock decay. The shorter window (Fig. 2b) reveals an accelerating rate of seismicity close to the mainshock epicentres during the hour immediately preceding the mainshock origin times.

## Earthquake triggering model

The anomalous nature of the RTF foreshock activity can be quantified in terms of the Epidemic Type Aftershock Sequence (ETAS) model of triggered seismicity<sup>4,29,30</sup>. ETAS is a marked point process model<sup>31</sup> in which all earthquake magnitudes above a lower cutoff  $m_0$  are independent samples of the Gutenberg–Richter (GR) probability distribution,  $P(m) = 10^{-b(m-m_0)}$ , where  $b$  is the slope of the distribution, and all earthquakes give birth to daughter events at

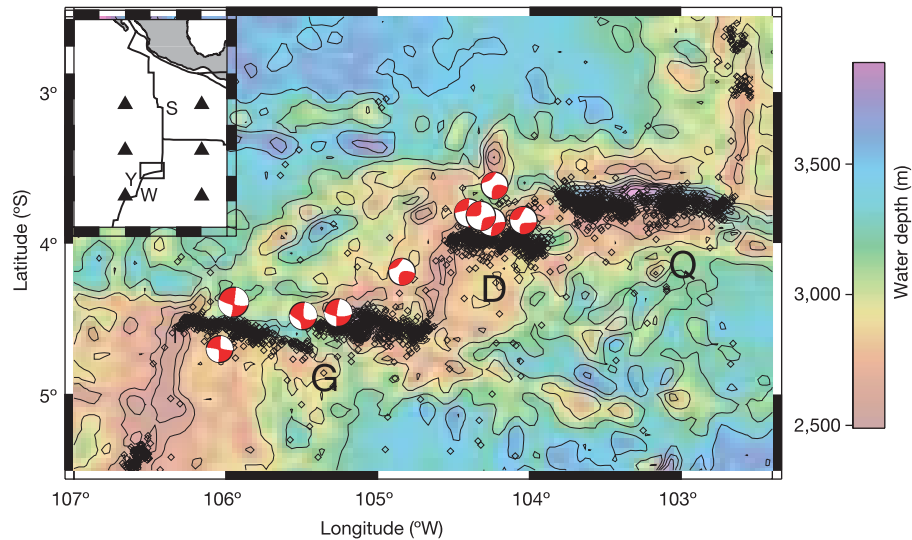


**Figure 1** Map of the Quebrada (Q), Discovery (D), and Gofar (G) transform faults in the equatorial eastern Pacific, contoured with the bathymetry predicted from the satellite-derived gravity field<sup>42</sup>. Diamond symbols represent the acoustic radiator positions in the NOAA-PMEL seismicity catalogue for 1996–2001<sup>24</sup>, and beachball symbols show the

focal mechanisms and centroid locations for the same period from the Harvard CMT catalogue. The inset map locates the EPR and Cocos ridge crests (black lines), the six NOAA hydrophones (triangles), the Wilkes (W), Yaquina (Y), and Siqueiros (S) transform faults, and the region of the main map (rectangle). The contour interval is 200 m.

an average rate of  $\phi(m, t) = \rho(m)\psi(t)$ , where  $t$  is time since the earthquake. This triggering rate is assumed to increase exponentially with magnitude,  $\rho(m) = k \times 10^{\alpha(m-m_0)}$ , where  $\alpha$  is the triggering exponent, and to decay with time after a mother event according to the modified Omori law,  $\psi(t) = \theta c^\theta / (c + t)^{1+\theta}$  (where  $\theta > 0$ ). The constants  $k$ ,  $\theta$  and  $c$  are parameters that vary among regions. Renormalization for a single mainshock of magnitude  $m$  yields an average seismicity rate proportional to<sup>29</sup>  $N_a^{II}(m) = \frac{k}{1-n} 10^{\alpha(m-m_0)}$ .  $N_a^{II}$  is the expected number of aftershocks of any magnitude (type-II aftershocks; that is, not constrained to be smaller than  $m$ ), and the constant  $n = \int_0^1 \rho(\mu) dP(\mu) = kb/(b - \alpha)$  is the branching ratio, which equals both the average number of directly triggered aftershocks per event and the fraction of the earthquake population

that is made up of triggered earthquakes<sup>30</sup>. The aftershock rate decays with an effective Omori exponent<sup>4</sup>  $p = 1 + O(\theta)$ .

In the ETAS model, the seismicity rate before a mainshock at  $t = 0$  increases according to the inverse Omori law; that is,  $\sim |t|^{-p'}$ , where  $p' = 1 + O[\theta]$ , and the expected number of events of all magnitudes conditioned on the mainshock occurrence (type-II foreshocks) is independent<sup>4</sup> of  $m$ . This conditional foreshock number can be approximated as the product of two factors: the probability that the mainshock is a triggered event, and the expected number of events in a cluster averaged over mainshock magnitude. The first is just the branching ratio  $n$ , and the second is the integral  $\int_0^1 N_a^{II}(\mu) dP(\mu)$ ; therefore<sup>30</sup>,  $N_f^{II} \approx n^2 / (1 - n)$ . To include only earthquakes smaller than the mainshock (type-I foreshocks), we multiply the integrand by the probability that no event in a cluster exceeds  $m$  and integrate over the appropriate magnitude range. If  $k/(1 - n)$  is small and  $m$  is large (conditions which apply to our data), then the extra probability factor is close to unity, and the results are  $N_f^I \approx N_f^{II} [1 - 10^{-(b-\alpha)(m-m_0)}]$ .

A similar modification to the aftershock number yields the foreshock/aftershock ratio:

$$\frac{N_f}{N_a} \approx n \left( \frac{b}{b - \alpha} \right) \left[ \frac{10^{(b-\alpha)\Delta m_1^f} - 10^{(b-\alpha)\Delta m_2^f}}{10^{b\Delta m_1^a} - 10^{b\Delta m_2^a}} \right] \quad (1)$$

Here we have generalized the formula to count foreshocks in the magnitude range from  $m - \Delta m_1^f$  to  $m - \Delta m_2^f$  and aftershocks from  $m - \Delta m_1^a$  to  $m - \Delta m_2^a$ , where  $0 \leq \Delta m_2^{f,a} < \Delta m_1^{f,a} \leq m - m_0$ . This approximation, which applies to large mainshocks, differs conceptually from the expression recently used by ref. 3 to explain the foreshock/aftershock ratios from global and regional catalogues (see Methods).

**Anomalous foreshock activity**

Earthquake populations on RTFs are well described by a tapered GR distribution having a low-magnitude slope  $b \approx 1$  (refs 14, 15) similar to that of continental regions. The hydroacoustic catalogue for the EPR faults is consistent with this self-similar scaling, and its aftershock sequences decay according to Omori’s law with<sup>32</sup>  $p \approx 1$ , again similar to continental regions. However, global catalogues demonstrate that the aftershock productivity of large RTF earthquakes is lower than continental faults by approximately a factor of fifteen<sup>15</sup> (Fig. 3). The low aftershock productivity combined with

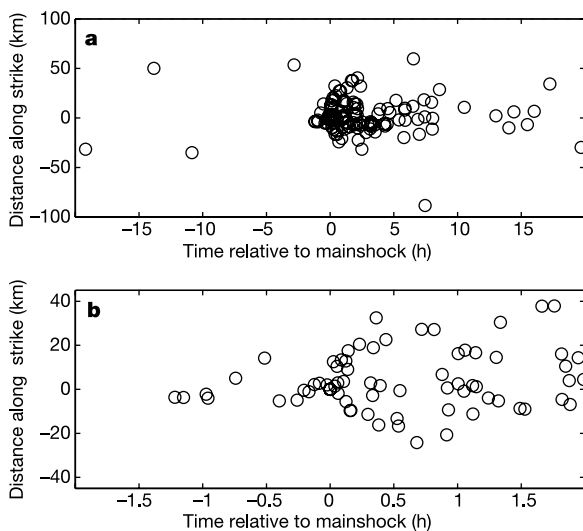


**Figure 2** Space-time distribution of seismicity around the nine mainshocks ( $M_w \geq 5.4$ ) on the Discovery and Gofar transform faults between May 1996 and December 2001, from the declustered Harvard CMT catalogue. **a**, Stack of all events from the NOAA-PMEL hydroacoustic catalogue with  $M_{ASL} > 2.5$  (for  $ASL > 207$ ) that were located within  $\pm 100$  km along strike and within  $\pm 20$  h of the mainshocks. Positive distance is west of the mainshock, and positive time is after the mainshock. **b**, Zoomed-in view of the same seismicity, showing foreshock activity within about 1 h and 15 km of the mainshocks.

the poor detection thresholds of global catalogues makes it difficult to constrain the values of  $n$  and  $\alpha$  independently. A maximum-likelihood fit to the teleseismic RTF data yields a best-fit value of the triggering exponent  $\alpha = 0.72$ , and is consistent with the somewhat higher values found for California and Japan ( $\alpha = 0.8-1.0$ )<sup>33,34</sup> (Fig. 3). Error bounds on the maximum-likelihood estimate are large, but aftershock counts using the hydroacoustic catalogue (points with horizontal bars in Fig. 3) also favour relatively high values of  $\alpha$  and rule out values less than about 0.6 (see Supplementary Information).

The difference between oceanic and continental aftershocks primarily manifests itself in the intercept of the scaling relation,  $k/(1-n)$ , which is offset by about a factor of fifteen (Fig. 3). The maximum-likelihood fit in Fig. 3 corresponds to a branching ratio,  $n \approx 0.1$ , compared to values approaching unity in continental seismic zones<sup>35</sup>. As discussed in the Supplementary Information, the aftershock rate may be somewhat higher for the EPR faults, but we can say with a high degree of confidence that  $n < 0.3$ . In other words, according to the ETAS model, most RTF earthquakes (70–90%) would be primary events driven by aseismic plate-tectonic loading rather than aftershocks of previous earthquakes. Equation (1) with the maximum-likelihood estimate of  $\alpha$  and  $n$  predicts that the foreshock/aftershock ratio for RTFs should be about an order of magnitude lower than that observed in continents.

Instead, the EPR transform faults that are well recorded by the NOAA-PMEL array give values of  $N_f/N_a$  that are an order of magnitude higher than observed in Southern California (Fig. 4). For both regions, we identified mainshocks as events in the Harvard CMT catalogue with  $M_w \geq 5.4$  that did not follow within 1 week and 100 km of another mainshock (see Methods), and we compiled

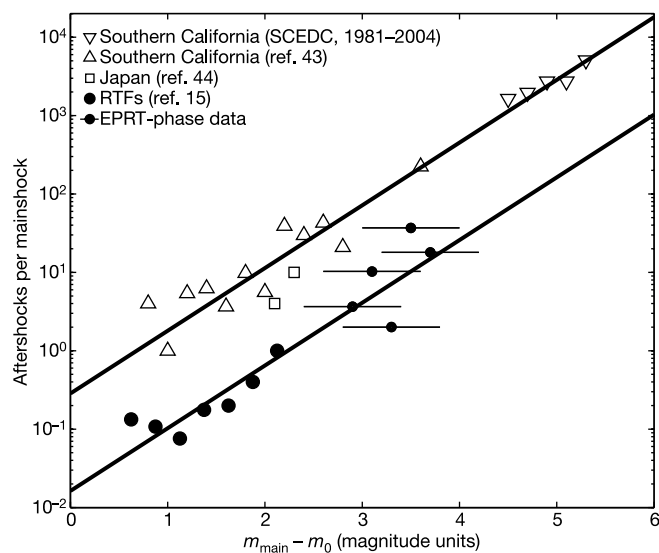


**Figure 3** Aftershocks per mainshock, plotted against the difference between the mainshock magnitude  $m_{\text{main}}$  and the catalogue completeness threshold  $m_0$ . RTF aftershocks (large filled circles) were defined as events with calibrated surface-wave magnitudes above  $m_0 = 5.1$  that occurred within 14 days and 100 km of a  $M_w \geq 5.6$  mainshock during the catalogue interval 1976–2001 (ref. 15). Southern California aftershocks from the SCEDC catalogue (open triangles) were defined as events above a local-magnitude ( $M_L$ ) threshold of  $m_0 = 2.0$  that occurred within 14 days and 100 km of a  $M_L \geq 6.5$  mainshock during the interval 1981–2004. Aftershock counts from the EPR  $T$ -phase catalogue (small filled circles) are shown with error bars to account for uncertainties in  $m_0$  ( $2.0 \leq m_0 \leq 3.0$ ). The  $T$ -phase catalogue aftershocks were counted within 14 days and 30 km of the mainshocks. Previously published continental data sets (open triangles and squares) were compiled by Kisslinger and Jones<sup>43</sup> and Yamanaka and Shimazaki<sup>44</sup> using  $M_L$  thresholds of  $m_0 = 4.0$  and  $4.5$ , respectively. Both RTF and continental aftershocks are consistent with a triggering exponent of  $\alpha = 0.8$  (solid lines), but RTFs produce fewer aftershocks by a factor of fifteen.

foreshock and aftershock statistics from the NOAA-PMEL and the Southern California Earthquake Data Center (SCEDC) catalogues. We counted all events with local magnitudes ( $M_{\text{ASL}}$  or  $M_L$ ) up to 2.8 units smaller than the mainshock  $M_w$  in the 1-h interval before and the 5-h interval after the mainshock. Figure 4 compares the observed  $N_f/N_a$  for spatial windows of various radii with the predictions of equation (1), corrected for the finite sampling intervals (see Methods). The SCEDC statistics satisfy an ETAS model with  $\alpha = 0.8-0.9$ , consistent with previous catalogue studies<sup>3,29</sup>. However, foreshock rates from the NOAA-PMEL statistics are about two orders of magnitude greater than the ETAS predictions using the maximum-likelihood fit in Fig. 3. As shown in Fig. 4 and Supplementary Fig. S3, these results are robust with respect to the choice of windows and declustering procedures.

Therefore, we can reject the ETAS hypothesis that the clustering of foreshocks, mainshocks and aftershocks on RTFs can be described by the same seismic triggering mechanism. We infer that large earthquakes on EPR faults are preceded by an extended preparation process, possibly driven by subseismic transients (silent or quiet earthquakes), that can often be observed through foreshocks. This alternative hypothesis is consistent with the tightly localized distribution of the foreshocks about the mainshock in both space and time (Fig. 2 and Supplementary Fig. S4), which does not conform to the inverse-diffusive behaviour expected from the ETAS model<sup>4</sup>.

The correspondence of slow slip with foreshocks was suggested as early as 1976 by Kanamori and Stewart<sup>18</sup>, who noted a foreshock with a body-wave magnitude  $m_b \approx 5$  about 500 s before the  $M_w = 7$  slow earthquake on the Gibbs transform fault in the North Atlantic. More recently, McGuire *et al.* associated  $m_b = 4.5-5.0$  foreshocks before the 1994  $M_w = 7.0$  Romanche<sup>20</sup> and 1997  $M_w = 6.8$  Prince Edward Island<sup>21</sup> earthquakes with slow precursors observed at low frequencies. Forsyth *et al.*<sup>22</sup> suggested

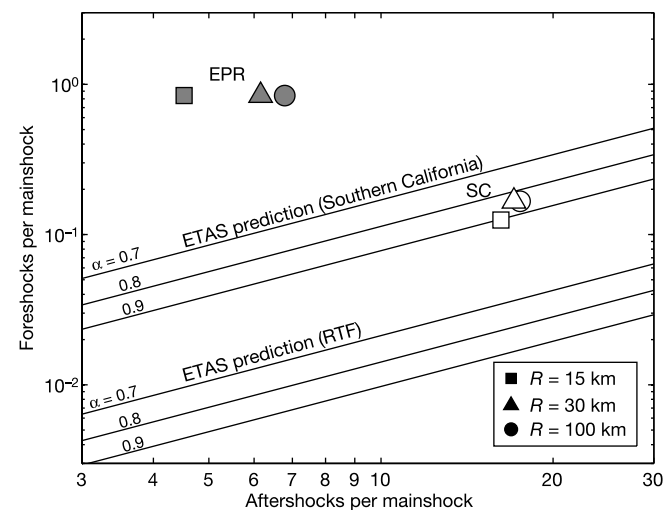


**Figure 4** Foreshock and aftershock rates observed for EPR transform faults (solid symbols) and Southern California (open symbols) in regions of radius  $R$  about the mainshock. The data sets included 19 mainshocks ( $M_w \geq 5.4$ ) on five transform faults (Discovery, Gofar, Wilkes, Yaquina and Siqueiros) from the declustered Harvard CMT catalogue for 1996–2001, and 24 mainshocks ( $M_L \geq 5.4$ ) in Southern California from the declustered SCEDC catalogue for 1981–2003. Events with magnitudes up to 2.8 units below the mainshock magnitude were counted from the NOAA-PMEL and SCEDC catalogues in the 1-h window preceding and 5-h window following the mainshocks. These rates are compared with the  $N_f/N_a$  ratios from the ETAS model (equation (1)) for  $\alpha = 0.7-0.9$  (solid lines), assuming  $\Delta m_2^{f,a} = 0$ ,  $\Delta m_1^{f,a} = 2.8$  and  $b = 1$ , with estimated branching ratios of  $n = 0.8$  (Southern California) and  $n = 0.1$  (RTF). The  $\alpha = 0.8$  line for RTFs is close to the maximum-likelihood estimate from Fig. 3. Uncertainties in  $\alpha$  and  $n$  allow shifts in the ETAS prediction upwards from the maximum-likelihood value by half an order of magnitude at most.

that a subseismic slip process was responsible for a swarm of contemporaneous seismicity on the Anakena and Raraku transform faults of the southern EPR recorded by an ocean-bottom seismometer array in 1995. These and other examples<sup>36</sup> combined with the global aftershock depletion (Fig. 3) and the evidence for slow precursors to large earthquakes on RTFs worldwide<sup>19</sup>, indicate that the aseismic, foreshock-generating process on EPR faults may be prevalent throughout the mid-ocean-ridge system, including the slower-slipping, colder RTFs in the Atlantic and Indian oceans.

**Short-term predictability of large earthquakes**

The high rate of proximate foreshocks suggests a naive scheme for short-term earthquake prediction—we simply assume that every event is a foreshock of an impending large earthquake. We can formalize this scheme into a well-posed prediction algorithm<sup>37</sup>: whenever we observe any RTF event above some ASL magnitude threshold  $m_0$  within a specified RTF region, we issue an alert that an earthquake of moment magnitude greater than or equal to  $m_p$  will occur sometime during time window of length  $t_p$  immediately following the event and somewhere in a spatial window of radius  $r_p$  about the event’s epicentre. Figure 5 illustrates this prediction algorithm for the parameter set [ $m_0 = 2.5$  ( $M_{ASL}$ ),  $m_p = 5.4$  ( $M_W$ ),  $t_p = 1$  h,  $r_p = 15$  km] by applying it retrospectively to the two most active EPR transform faults, Discovery and Gofar. Of the nine candidate earthquakes that occurred during the catalogue interval May 1996–November 2001, six were located within the space-time prediction windows (Fig. 5) and thus constitute successful predictions. There were three failures-to-predict and about 1,400 false alarms.

Although the false-alarm rate is quite high, all alarms taken together occupy only about 0.15% of the total space-time volume of about 250 km × 5.5 yr (see Supplementary Information). We can relate  $P(M|F)$ , the probability of a mainshock  $M$  in the prediction window given the occurrence of a foreshock  $F$ , to  $P(M)$ , the probability of  $M$  in a random window of the same size, using the Bayes identity:

$$P(M|F) = P(M) \left[ \frac{P(F|M)}{P(F)} \right] \tag{2}$$

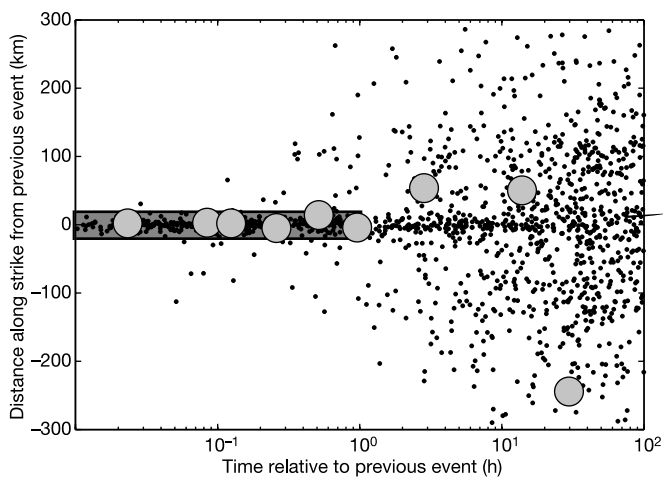


**Figure 5** Retrospective application of the naive prediction algorithm described in the text to the NOAA-PMEL catalogue (May 1996–November 2001) for the Discovery and Gofar faults. Plot shows along-strike distance (positive to the west) and time of each earthquake relative to its previous event for all catalogued events with  $M_{ASL} \geq 2.5$  ( $ASL \geq 207$ ). Events were considered to be distinct if they were separated by more than 1 min from the previous event, to exclude redundancies. Six of the nine mainshocks identified from the declustered Harvard CMT catalogue (large circles) fall within the 1-h, ±15-km alert windows (shaded area) used in the prediction algorithm.

$P(F|M)$  is the fraction of mainshocks preceded by foreshocks, and  $P(F)$  equals the fraction of the space-time volume occupied by alerts. The ratio of these probabilities (the term in square brackets) is the probability gain factor  $g$  of the prediction algorithm<sup>37</sup>. Our retrospective analysis of the Discovery and Gofar faults gives  $g = 450$ . This performance can be compared to prediction experiments in California, where even highly optimized algorithms with many adjustable parameters are thought to achieve probability gains of 10–20 or less<sup>38</sup>.

The performance relative to random chance can be evaluated using Molchan’s<sup>39</sup> error diagram, which plots the failure-to-predict probability,  $1 - P(F|M)$ , against  $P(F)$  (Fig. 6). Large sets of random alerts should fall close to the line  $1 - P(F)$ , corresponding to no probability gain ( $g = 1$ ). Figure 6 shows that the Discovery–Gofar point lies well below the 99% confidence range for random chance; the probability of reproducing this performance with random alerts filling 0.15% of the space-time volume is less than one in ten million. Similar results were obtained by applying the algorithm retrospectively to the five active EPR transforms in the study area; nine of sixteen mainshocks were successfully predicted by alerts occupying 0.13% of the space-time volume, which gives  $g = 340$  (Fig. 6, see Supplementary Discussion).

Our naive algorithm is far from optimal. For instance, raising the threshold magnitude  $m_0$  from 2.5 to 3.4 (that is, increasing the ASL from 207 to 215) reduces the number of alarms in the Gofar–Discovery catalogue to 407 without changing  $P(F|M)$ , increasing  $g$  to about 1,000 (Fig. 6). More parameters could be added to improve the performance further.

**Discussion**

Mid-ocean ridges are far removed from urban centres on continents, so the direct societal value of short-term earthquake prediction on RTFs (assuming it could be operationally implemented using real-time, near-source monitoring) would be small. Nevertheless, the existence of short-term predictability in this tectonic environment—the main conclusion of this paper—is of considerable scientific interest, because it supports a physical linkage between foreshocks and mainshocks through stress changes driven by aseismic slip transients or some other fault preparation process

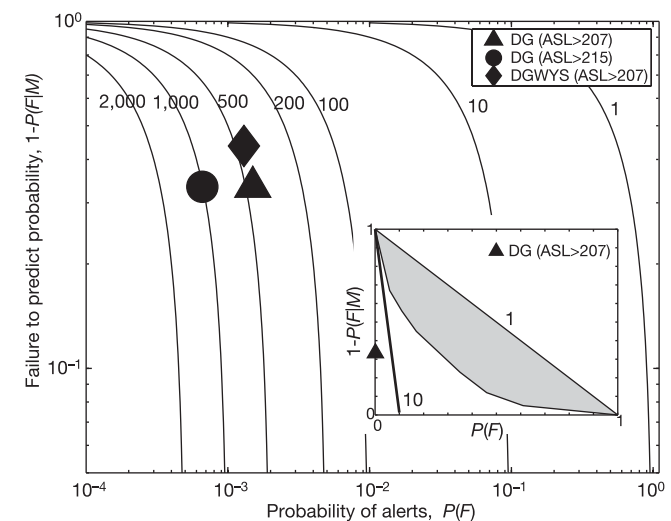


**Figure 6** Molchan’s<sup>39</sup> error diagram of the failure-to-predict probability  $1 - P(F|M)$  against the probability of alerts  $P(F)$  on a logarithmic scale, contoured with probability gain  $g$  (solid curves). Performance of the naive prediction algorithm is given for the Discovery and Gofar (DG) faults with  $m_0 = 2.5$  (triangle) and  $m_0 = 3.4$  (circle), and for the five active EPR faults (DGWYS) with  $m_0 = 2.5$  (diamond). Inset diagram is the same plot on a linear scale, comparing the 99% confidence region for a random prediction of nine mainshocks (shaded area) with the first DG test (triangle).

such as hydrothermal flow or nearby magmatic activity.

To monitor RTFs geodetically will require a new generation of ocean-bottom instrumentation, a considerable technological challenge. But collecting such data may well be the best way to test the hypothesis that three anomalous aspects of RTF seismicity—large slip deficits, high foreshock activity and slow earthquakes—can be explained by aseismic fault-slip transients. Given the importance of understanding the fundamental mechanics of earthquake predictability, overcoming the technological hurdles should be worth the effort. □

Methods

We use the NOAA-PMEL hydroacoustic earthquake catalogue for the equatorial Pacific which began in 1996 (ref. 24). Their array (Fig. 1) records acoustic energy radiated into the water column by earthquakes and other sources (*T*-phases). *T*-phases propagate very efficiently in the low-velocity sound fixing and ranging (SOFAR) channel, and the array arrivals can be used to locate precisely where the energy entered the SOFAR channel. The standard errors in this source location are estimated to be ±2 km, ±10 s for the southern/northernmost faults (the Wilkes and Siqueiros faults) and are slightly smaller for the faults located in the centre of the array<sup>24</sup> (the Discovery and Gofar faults). A propagation model is used to convert the magnitude of the pressure signal at the hydrophones into an ASL (measured in decibels) at the source location. We used a conversion between ASL and magnitude,  $M_{ASL} = 0.107ASL - 19.6$ , obtained from the regression of the observed ASLs compiled in ref. 32 against the body-wave magnitudes of the International Seismological Centre (ISC) catalogue (<http://www.isc.ac.uk/>). Frequency-magnitude statistics indicate that the seismicity catalogues are approximately complete down to  $ASL \approx 207\text{--}212$ , or  $M_{ASL} \approx 2.5\text{--}3.0$ .

To prevent biases from ongoing aftershock sequences, we eliminated CMT catalogue earthquakes that occurred within 1 week and 100 km of a previous CMT earthquake from our analysis. Our de-clustering criterion eliminated only one earthquake with  $M_w \geq 5.5$  from the Discovery–Gofar set and only two from the mainshock set for other three active RTFs within the NOAA-PMEL array. Moderate increases in the space and time windows did not disqualify additional events. Moreover, each of the three disqualified events had a foreshock sequence distinct from the aftershock sequence of the preceding mainshock, consistent with the statistics in Fig. 4 (see Supplementary Fig. 2).

The time dependence of foreshock and aftershock rates in ETAS is controlled by Omori's law. Helmstetter *et al.*<sup>4</sup> have demonstrated that the time-decay exponent *p* in the renormalized Omori law is not strictly a constant. When  $\rho(m)$  has finite variance ( $\alpha/b \leq 1/2$ ), *p* varies from  $1 - \theta$  for  $t \ll t^* = c(n/|1 - n|)^{1/\theta}$  to  $1 + \theta$  for  $t \gg t^*$ . The theory breaks down for  $\alpha/b > 1/2$ , owing to the strong coupling between earthquake energy and seismicity rate, but the numerical simulations of ref. 4 indicate that the short-time value of *p* increases approximately linearly from  $1 - \theta$  at  $\alpha/b = 1/2$  to  $1 + \theta$  as  $\alpha/b \rightarrow 1$ . For  $\alpha/b = 0.8$ , the Omori exponents can be approximated by  $p' \approx p \approx 1 + \theta$ ; hence, the requisite integrals are  $\int_0^{\Delta t_{f,a}} \psi(\tau) d\tau \approx 1 - (c/\Delta t_{f,a})^\theta$ , where the approximation assumes  $\Delta t_{f,a} \gg c$ . Equation (1) can thus be corrected for the finite foreshock and aftershock sampling intervals,  $\Delta t_f = 1$  h and  $\Delta t_a = 5$  h, by multiplying its right-hand side by the ratio of these integrals. This ratio varies from 0.72 to 0.94 over the plausible range of parameters  $c = 1$  s – 1 min,  $\theta = 0\text{--}0.2$ , so the correction is minor.

Equation (1) is a more general form of models used in previous studies<sup>3,12,40,41</sup>. Feltzer *et al.*<sup>3</sup> consider the case  $\alpha = b$ . Taking this limit in equation (1), we obtain  $N_f/N_a \approx n(\ln 10) \left[ \frac{\Delta m_f^2 - \Delta m_a^2}{10^{0.25\Delta m_f^2} - 10^{0.25\Delta m_a^2}} \right]$ . For the magnitude ranges of ref. 3 ( $\Delta m_f^2 = 1.0$ ,  $\Delta m_a^2 = 0$ ;  $\Delta m_f^2 = 1.0$ ,  $\Delta m_a^2 = 0.4$ ), the ratio in brackets reproduces their foreshock/aftershock ratio of 0.134. The factor  $n(\ln 10)$  missing in their equation (6) probably lies between 1 and 2 for continental and subduction-zone seismicity<sup>30</sup>, so their formula provides an adequate approximation in most regions. For RTFs, however, the scaling of  $N_f/N_a$  with the branching ratio *n* is numerically important (see Fig. 4).

Received 3 September 2004; accepted 19 December 2005; doi:10.1038/nature03377.

1. Jones, L. M. & Molnar, P. Some characteristics of foreshocks and their possible relationship to earthquake prediction and premonitory slip on faults. *J. Geophys. Res.* **84**, 3596–3608 (1979).
2. Abercrombie, R. E. & Mori, J. Occurrence patterns of foreshocks to large earthquakes in the Western United States. *Nature* **381**, 303–307 (1996).
3. Felzer, K., Abercrombie, R. E. & Ekstrom, G. A common origin for aftershocks, foreshocks, and multiplets. *Bull. Seismol. Soc. Am.* **94**(1), 88–98 (2004).
4. Helmstetter, A., Sornette, D. & Grasso, J.-R. Mainshocks are aftershocks of conditional foreshocks: How do foreshock statistical properties emerge from aftershock laws. *J. Geophys. Res.* **108**, doi:10.1029/2002JB001991 (2003).
5. Dodge, D. A., Ellsworth, W. E. & Beroza, G. C. Detailed observations of California foreshock sequences: Implications for the earthquake initiation process. *J. Geophys. Res.* **101**, 22371–22392 (1996).
6. Geller, R. J., Jackson, D. D., Kagan, Y. Y. & Mulargia, F. Earthquakes cannot be predicted. *Science* **275**, 1616–1617 (1997).
7. Hirose, H., Hirahara, K., Kimata, F., Fujii, N. & Miyazaki, S. A slow thrust slip event following the two 1996 Hyuganada earthquakes beneath the Bungo Channel, Southwest Japan. *Geophys. Res. Lett.* **26**, 3237–3240 (1999).
8. Ozawa, S. *et al.* Detection and monitoring of ongoing aseismic slip in the Tokai region, central Japan. *Science* **298**, 1009–1012 (2002).
9. Ozawa, S. *et al.* Characteristic silent earthquakes in the eastern part of the Boso peninsula, Central Japan. *Geophys. Res. Lett.* **30**, doi:10.1029/2002GL016665 (2003).
10. Dragert, H., Wang, K. & James, T. S. A silent slip event on the deeper Cascadia subduction interface. *Science* **292**, 1525–1528 (2001).

11. Kanamori, H. & Cipar, J. Focal process of the great Chilean earthquake. *Phys. Earth Planet. Inter.* **9**, 128–136 (1974).
12. Reasenber, P. A. Foreshock occurrence before large earthquakes. *J. Geophys. Res.* **104**, 4755–4768 (1999).
13. Brune, J. N. Seismic moment, seismicity, and rate of slip along major fault zones. *J. Geophys. Res.* **73**, 777–784 (1968).
14. Bird, P., Kagan, Y. & Jackson, D. in *Plate Boundary Zones* (ed. Freymueller, S. S. A. J.) 203–218 (AGU, Washington DC, 2002).
15. Boettcher, M. S. & Jordan, T. H. Earthquake scaling relations for mid-ocean ridge transform faults. *J. Geophys. Res.* **109**, doi:10.1029/2004JB003110 (2004).
16. Bird, P. & Kagan, Y. Plate-tectonic analysis of shallow seismicity: Apparent boundary width, beta, corner magnitude, coupled lithosphere thickness, and coupling in 7 tectonic settings. *Bull. Seismol. Soc. Am.* **94**(6), 2380–2399 (2004).
17. Perez-Campos, X., McGuire, J. J. & Beroza, G. C. Resolution of the slow earthquake/apparent stress paradox for oceanic transform fault earthquakes. *J. Geophys. Res.* **108**, doi:10.1029/2002JB002312 (2003).
18. Kanamori, H. & Stewart, G. S. Mode of strain release along the Gibbs fracture zone, Mid-Atlantic Ridge. *Phys. Earth Planet. Inter.* **11**, 312–332 (1976).
19. Ihlmlé, P. F. & Jordan, T. H. Teleseismic search for slow precursors to large earthquakes. *Science* **266**, 1547–1551 (1994).
20. McGuire, J. J., Ihlmlé, P. F. & Jordan, T. H. Time-domain observations of a slow precursor to the 1994 Romanche transform earthquake. *Science* **274**, 82–85 (1996).
21. McGuire, J. J. & Jordan, T. H. Further evidence for the compound nature of slow earthquakes: The Prince Edward Island earthquake of April 28, 1997. *J. Geophys. Res.* **105**, 7819–7828 (2000).
22. Forsyth, D. W., Yang, Y., Mangriotis, M.-D. & Shen, Y. Coupled seismic slip on adjacent oceanic transform faults. *J. Geophys. Res.* **30**, doi:10.1029/2002GL016454 (2003).
23. Abercrombie, R. E. & Ekstrom, G. Earthquake slip on oceanic transform faults. *Nature* **410**, 74–77 (2001).
24. Fox, C. G., Matsumoto, H. & Lau, T. K. Monitoring Pacific Ocean seismicity from an autonomous hydrophone array. *J. Geophys. Res.* **163**, 4183–4206 (2001).
25. Fox, C. G. *et al.* Acoustic detection of seafloor spreading. *J. Geophys. Res.* **22**, 131–134 (1995).
26. Smith, D. *et al.* Hydroacoustic monitoring of seismicity at the slow-spreading Mid-Atlantic Ridge. *Geophys. Res. Lett.* **29**, doi:10.1029/2001GL013912 (2002).
27. McGuire, J. J. Immediate foreshock sequences of oceanic transform earthquakes on the East Pacific Rise. *Bull. Seismol. Soc. Am.* **93**, 948–952 (2003).
28. Ekstrom, G., Dziewonski, A. M., Maternovskaya, N. N. & Nettles, M. Global seismicity of 2001; centroid-moment tensor solutions for 961 earthquakes. *Phys. Earth Planet. Inter.* **136**, 165–185 (2003).
29. Helmstetter, A. & Sornette, D. Bath's law derived from the Gutenberg-Richter law and from aftershock properties. *Geophys. Res. Lett.* **30**, doi:10.1029/2003GL018186 (2003).
30. Helmstetter, A. & Sornette, D. Importance of direct and indirect triggered seismicity in the ETAS model of seismicity. *Geophys. Res. Lett.* **30**, 4, doi:10.129/2003GL017670 (2003).
31. Ogata, Y. Statistical models for earthquake occurrence and residual analysis for point processes. *J. Am. Stat. Assoc.* **83**, 9–27 (1988).
32. Bohnenstiehl, D. R., Tolstoy, M., Dziak, R. P., Fox, C. G. & Smith, D. Aftershocks in the mid-ocean ridge environment: An analysis using hydroacoustic data. *Tectonophysics* **354**, 49–70 (2002).
33. Helmstetter, A. Is earthquake triggering driven by small earthquakes? *Phys. Rev. Lett.* **91**, 058501 (2003).
34. Helmstetter, A., Kagan, Y. & Jackson, D. D. Importance of small earthquakes for stress transfers and earthquake triggering. *J. Geophys. Res.* (in press).
35. Helmstetter, A. & Sornette, D. Subcritical and supercritical regimes in epidemic models of earthquake aftershocks. *J. Geophys. Res.* **107**, doi:10.1029/2001JB001580 (2002).
36. Hanson, J. A. & Given, H. K. Accurate azimuth estimates from a large aperture hydrophone array using T-phase waveforms. *Geophys. Res. Lett.* **25**, 365–368 (1998).
37. Aki, K. in *Earthquake Prediction* (eds Simpson, D. W. & Richards, P. G.) 556–574 (AGU, Washington DC, 1981).
38. Keilis-Borok, V., Shebalin, P., Gabrielow, A. & Turcotte, D. Reverse tracing of short-term earthquake precursors. *Phys. Earth Planet. Inter.* **145**, 75–85 (2004).
39. Molchan, G. M. Earthquake prediction as a decision-making problem. *Pure Appl. Geophys.* **149**, 233–247 (1997).
40. Reasenber, P. A. & Jones, L. M. Earthquake hazards after a mainshock in California. *Science* **243**, 1173–1176 (1989).
41. Reasenber, P. A. & Jones, L. M. Earthquake aftershocks: Update. *Science* **265**, 1251–1252 (1994).
42. Sandwell, D. T. & Smith, W. H. F. Marine gravity anomaly from Geosat and ERS 1 satellite altimetry. *J. Geophys. Res.* **102**, 10039–10054 (1997).
43. Kisslinger, C. & Jones, L. M. Properties of aftershock sequences in Southern California. *J. Geophys. Res.* **96**, 11947–11958 (1991).
44. Yamanaka, Y. & Shimazaki, K. Scaling relationship between the number of aftershocks and the size of the main shock. *J. Phys. Earth* **38**, 305–324 (1990).

Supplementary Information accompanies the paper on [www.nature.com/nature](http://www.nature.com/nature).

**Acknowledgements** We thank R. Dziak for answering questions about details of the hydroacoustic earthquake catalogues, D. Bohnenstiehl for suggestions on clarifying the manuscript, A. Helmstetter for her help in understanding ETAS, and V. Keilis-Borok, I. Zaliapin, and L. Jones for discussions of earthquake prediction algorithms. J.J.McG. was supported by the Frank and Lisina Hoch Fund. M.S.B. was supported by the Deep Ocean Exploration Institute at WHOI. This work was supported by the NSF, SCEC and USGS.

**Competing interests statement** The authors declare that they have no competing financial interests.

**Correspondence** and requests for materials should be addressed to J.J.McG. ([jmcguire@whoi.edu](mailto:jmcguire@whoi.edu)).

## Supplementary Information

Supplementary Discussion:

Foreshocks and Aftershocks on EPR Faults

Declustering

Sensitivity to Parameter Choices

Estimation of  $\alpha$  and  $n$

Prediction Space-Time Windows

Supplementary Tables S1-S4

Supplementary Figs. S1-S4

### Foreshocks and aftershocks on EPR faults

The NOAA hydroacoustic array in the equatorial eastern Pacific detects earthquakes from much of the Pacific basin, but only six RTFs are contained within the region for which the array has both its maximum detection ability and location accuracy. The tectonic parameters of these faults are given in Table S1. Global RTF scaling relations<sup>15</sup> predict that the largest magnitude earthquake typically observed on this set of faults would be about  $M_w$  6.3. The Quebrada transform has not produced any earthquakes large enough for inclusion in the Harvard CMT catalog during the operation of the  $T$ -phase array (Fig. 1) and hence was not used in our foreshock analysis.

Fault	Latitude (°N)	Length (km)	Slip Velocity (mm/yr)	Seismic Coupling (%)
Siqueiros (S)	8.4	150	112	6
Quebrada (Q)	-3.8	120	137	1
Discovery (D)	-4.0	70	138	19
Gofar (G)	-4.5	190	139	12
Yaquina (Y)	-6.2	60	141	2
Wilkes (W)	-9.0	200	145	2

Table S1. Tectonic Parameters of the RTFs considered in this study. Seismic coupling estimates are taken from Boettcher and Jordan<sup>15</sup> for plate motion above the 600°C isotherm. The letters in parentheses following the fault names are used to refer to the various faults.

Table S2 lists all the earthquakes in both the Harvard CMT and NOAA catalogs for the EPR faults sorted by their magnitude. The events on the Yaquina, Wilkes, and Siqueiros transforms tend to be slightly smaller than the Discovery and Gofar events, but 3 of the 5 declustered mainshocks on these faults (i.e., events with  $M_W \geq 5.4$  that did not follow within 1 week and 100 km of another mainshock) had foreshocks in the 1-hr  $\times$  15-km window, consistent with the observations of Discovery and Gofar faults (6 of 9). Table S2 suggests that foreshocks are more likely for  $M_W \geq 5.5$  events (8 of 13) than for  $5.3 \leq M_W < 5.5$  events (2 of 6), but longer hydraulic catalogs will be required to confirm this trend.

CMT ID	Year	Day	Fault	$M_W$	$N_f$	$N_a$
080596D	1996	218	Y	5.3	0	3
051397A	1997	133	W	5.3	1	0
033199C	1999	090	W	5.3	0	5
042601D	2001	116	S	5.3	7*	9
072197B	1997	202	W	5.4	0	1
100898B	1998	281	W	5.4	0	4
102000B	2000	294	G	5.4	2	1
091899A	1999	261	G	5.5	0	5
091701D	2001	260	W	5.5	0	3
111099A	1999	314	Y	5.5	14	7
111598E	1998	319	D	5.5	1	7
081200B	2000	225	S	5.5	2	3
0730001B	2001	211	D	5.6	0	0
032597D	1997	084	G	5.6	1	0
042601C	2001	116	S	5.7	1	8
040797D	1997	097	G	5.7	0	1
082396D	1996	236	D	5.8	1*	5
051098C	1998	130	S	5.8	0	8
051198A	1998	131	S	5.8	11*	18
082396D	1996	236	D	5.9	3	2
062601H	2001	177	D	6.0	2	3
081597B	1997	227	G	6.2	2	12

Table S2. EPR earthquakes in both the Harvard CMT and NOAA-PMEL Catalogs. Foreshocks and aftershocks are events within  $\pm 15$  km and 1 hour of a mainshock, based on NOAA-PMEL locations. The source fault for each earthquake are denoted by W (Wilkes), S (Siqueiros), Y (Yaquina), D (Discovery), G (Gofar). Events with an

asterisk next to their foreshock counts are disqualified by the declustering algorithm used in the text; e.g., these mainshocks occurred within 1 week and 100 km of a previous mainshock.

Table S3 contains two earthquakes on the Gofar fault from July, 2002, that are not yet included in the NOAA-PMEL catalog. Inspection of the seismograms from the GSN station PAYG on the Galapagos Islands indicates that these events were preceded by a  $M_w$  5.0 earthquake in the 1 hour beforehand (Fig. S1). The ISC located the  $M_w > 5.0$  events on the Gofar fault. The NOAA-PMEL locations for these (and smaller) foreshocks will constitute a prospective test of our prediction algorithm in the time period following our 1996-2001 training set.

CMT ID	Year	Day	$M_w$	Fault	$N_f$	$N_a$
061702B	2002	168	5.8	G	1	3
061702C	2002	168	6.0	G	2	2

Table S3. Similar to table S2, but for events occurring after the current end of the NOAA catalog. These earthquakes are shown in Fig. S1.

## Declustering

Three earthquakes in Table S2 were not used in either Fig. 4 or 6 because they occur within 100 km and 1 week of a previous CMT earthquake, and thus their foreshock and aftershock counts are potentially elevated. While these events were disqualified to conform to standard catalog analysis, each event has a foreshock sequence that can be distinguished from the previous event's aftershock sequence. Fig. S2 shows the clear clusters of activity before the two Siqueiros events that are spatially and temporally distinct from the previous aftershock sequence. Thus, the three disqualified events also show evidence of the extended ( $\sim 1$  hr) fault preparation process implied by the sequences in Fig. 2. We did not attempt to decluster based on the ASL estimates provided by the NOAA-PMEL catalog because (1) these values show large scatter when correlated with surface-wave and moment magnitudes, and (2) for the typical aftershock sequence depicted in Fig. 3, the difference in magnitude between the mainshock and largest aftershock (Båth's law<sup>45,46</sup>) is typically 2.4 units. Therefore only mainshocks larger than magnitude 5.0 would contribute aftershocks to the  $T$ -phase catalog, which has detection threshold of 2.5-3.0. Thus, the foreshock counts in Table S2 are not likely to be

contaminated by aftershocks triggered by events too small to be included in the CMT catalog.

### **Sensitivity to Parameter Choices**

The observed foreshock/aftershock ratio in Fig. 4 depends on the temporal and spatial windows. Although 30 km windows are probably best for minimizing bias in this ratio, the results were found to be insensitive to variations in window size from 15 to 100 km (Fig. 4). Moreover, 30 kilometers corresponds to a clear dropoff in the spatial clustering in Fig. 2A, as well as being about twice the expected rupture length of the largest ( $M_w$  6.2) mainshock in our dataset. We tested the dependence of the foreshock/aftershock ratio on time windows up to a month long (Fig. S3). For Southern California events, the implied values of  $n$  were near 1, consistent with previous studies<sup>33,34</sup>, except for large foreshock time intervals, where foreshock counts were contaminated by background seismicity. Our conclusion that the foreshock/aftershock ratio for EPR faults is substantially larger than that for Southern California is robust with respect to large variations in spatial and temporal window lengths (Fig. S3).

### **Estimation of $\alpha$ and $n$**

The lack of a uniform magnitude scale for measuring RTF earthquakes over a wide range of sizes introduces uncertainties into the estimates of  $n$  and  $\alpha$  obtained from the magnitude dependence of aftershock rates. In Fig. 3, we used  $M_w$  from the Harvard CMT catalog to measure mainshock magnitude and  $M_S$  values from the ISC catalog, recalibrated against  $M_w$ <sup>15</sup>, to measure aftershock magnitude. A maximum-likelihood fit to these data gave  $n \approx 0.1$  for the global RTF data set (for  $\alpha = 0.72$ ), but the 95% confidence region of this fit is large. There are numerous mainshocks (more than 400 total) that control the end of the line at low values of  $m_{\text{main}} - m_0$ , but relatively few (about 20) with  $m_{\text{main}} - m_0 > 1.5$  to pin the high end of the curve.

The NOAA-PMEL catalog can be used to estimate the number of aftershocks at much smaller magnitudes than the global catalogs, and thus to constrain  $\alpha$ . We counted aftershocks on EPR transforms in the first day after the  $M_w \geq 5.7$  mainshocks, obtaining an average value of 59 per mainshock. The appropriate value of  $m_{\text{main}} - m_0$  to use with this frequency was highly uncertain, however, owing to the  $M_{\text{ASL}}$  uncertainty; according to published estimates, the detection threshold could be anywhere from about 1.8<sup>24</sup> to 2.9<sup>32</sup> with some claimed detections<sup>24</sup> as small as  $m_b$  0.5. We determined a very conservative lower bound on  $\alpha$  by assuming the NOAA-PMEL catalog is complete down to  $M_w$  1.0. Combining the EPR counts with the global RTF aftershock data from Fig. 3 in

the same maximum likelihood fit requires  $\alpha > 0.6$ . The EPR aftershock data do not provide a clear upper bound on  $\alpha$ , and even permit values greater than one, but the combination of the EPR and global RTF datasets constrain  $n$  to be smaller than about 0.3.

Another potential source of uncertainty is that the aftershock rates of EPR faults could be greater than the global RTF average. However, large earthquakes on the Blanco Transform of the Juan De Fuca Ridge also show similarly numerous small magnitude (hydroacoustically detected) aftershocks<sup>47</sup>, suggesting that relatively large values of  $\alpha$  characterize RTF behavior over a significant range in spreading rate.

### **Prediction Space-Time Windows**

The total space-time volume filled by the alerts was calculated by integrating the space-time window of each individual alert forward in time until either the time window expired or another earthquake occurred. This approach was necessary to avoid double counting many duplicate entries of small earthquakes in the catalog with origin times only a few seconds apart.

## SOM Figures

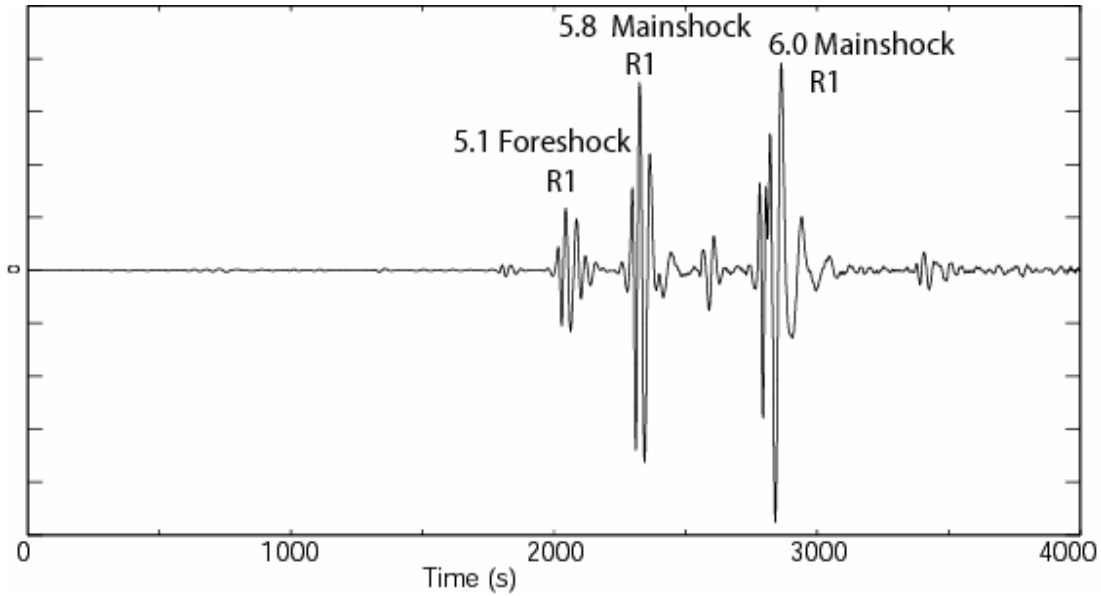


**Fig. S1.** Vertical component seismogram from station PAYG (Galapagos) for a 4000-s period on June 17, 2002, when a series of large earthquakes ruptured the Gofar fault (epicentral distance  $\approx 1000$  km). The Rayleigh-wave arrivals are labeled for four earthquakes, the last two of which have moment magnitudes listed in the Harvard CMT catalog. The arrivals are nearly identical at low frequencies, suggesting all three events ruptured the Gofar fault.

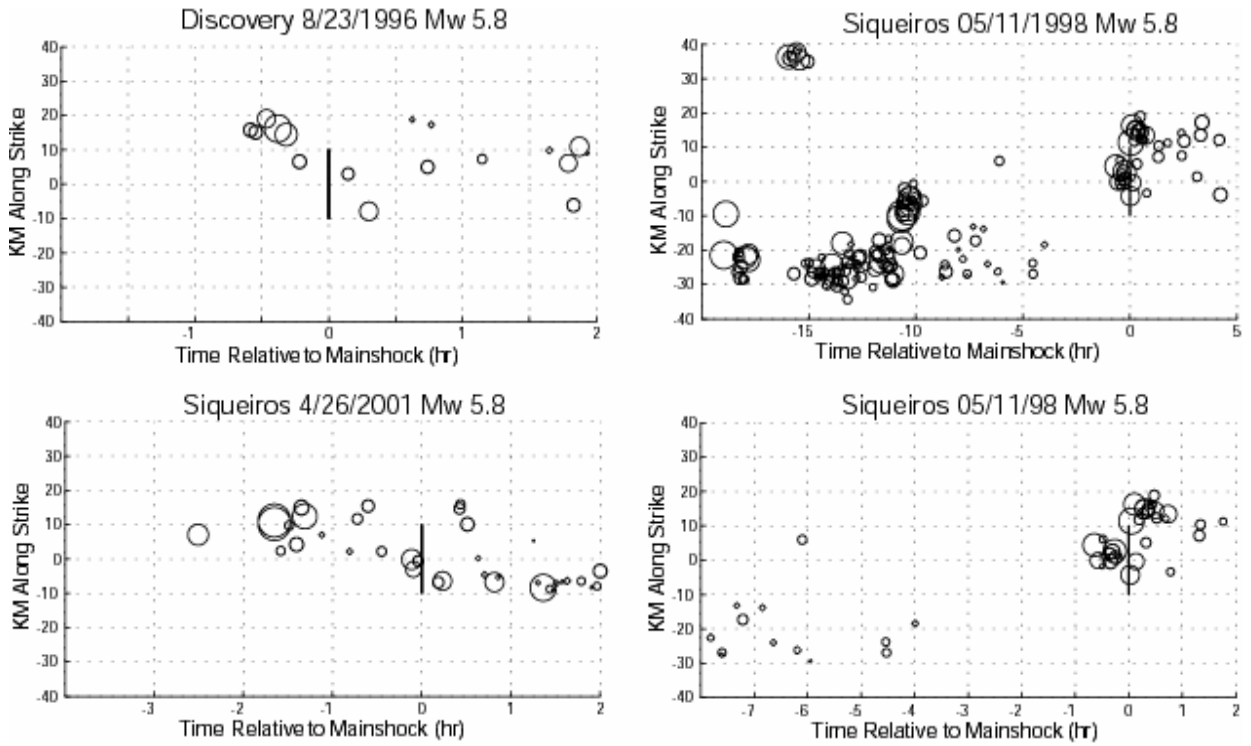


**Fig. S2.** Space-time plots of the seismicity surrounding the 3 CMT catalog events that were excluded by our declustering procedure (see methods). The plot is shown at two different scales for the 5/11/98 event. The symbol size is scaled according to the ASL for each event. The two Siqueiros events show foreshock sequences in the last half-hour before the mainshock that appear to be distinct from the aftershock sequence of the preceding event.

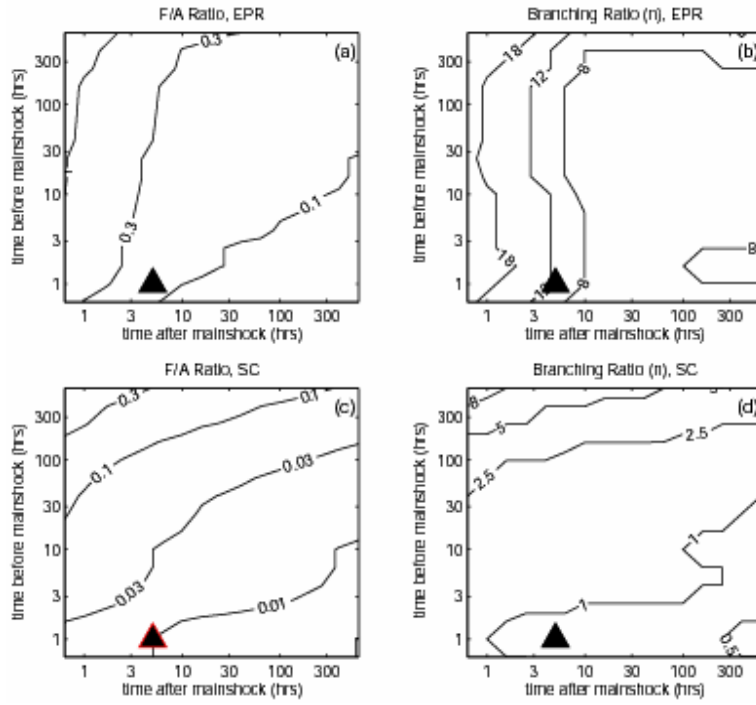


**Fig. S3.** Effect of time-window length on the observed foreshock/aftershock ratio. Results are shown for the 19 mainshocks from 5 active EPR faults in (A) and the 24 mainshocks from Southern California (SC) in (C). Foreshocks and aftershocks were counted within 15 km of the mainshock and in the magnitude range 0 to 2.8 units below the mainshock  $M_w$ . EPR events were taken from the NOAA-PMEL catalog and SC events were taken from the SCEDC catalog. The branching ratios for EPR events in (B) and for SC events in (D) were calculated from Eqn. 1 assuming  $\Delta m_2^{f,a} = 0$ ,  $\Delta m_1^{f,a} = 2.8$ ,  $b = 1$ , and  $\alpha = 0.8$ . Triangles show the window lengths used in Fig. 4.

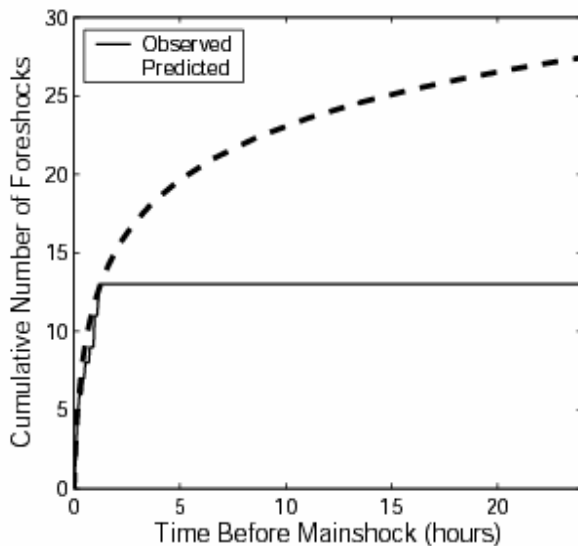


**Fig. S4.** A comparison of the inverse Omori law for  $p' = 1$  (dashed line) with the stacked foreshock sequences from Fig. 3 (solid line). The inverse Omori law provides a reasonable fit to the foreshock rate in a 1-hr period before the mainshocks, but it is inconsistent with the lack of any measurable foreshock activity before 1 hr.

#### Additional References

45. Bath, M. Lateral inhomogeneities in the upper mantle. *Tectonophysics* **2**, 483–514 (1965).
46. Richter, C. F. *Elementary Seismology* (Freeman, San Francisco, 1958).
47. Dziak, R. P. *et al.* Recent tectonics of the Blanco Ridge, eastern Blanco transform fault zone. *Mar. Geophys. Res.* **21**, 423–450 (2000).